Supporting Information for: Hydrogen Bonding Controls the Structural Evolution in Perovskite-Related Hybrid Platinum (IV) Iodides

Hayden A. Evans,[†,‡] Douglas H. Fabini,[¶,‡] Jessica L. Andrews,[†] Mitchell Koerner,[§] Molleigh B. Preefer,[†,‡] Guang Wu,[†] Fred Wudl,[¶] Anthony K. Cheetham,[‡,‖] and Ram Seshadri[*,†,¶,‡]

†*Department of Chemistry and Biochemistry*
University of California, Santa Barbara, California 93106, United States
‡*Materials Research Laboratory*
University of California, Santa Barbara, California 93106, United States
¶*Materials Department*
University of California, Santa Barbara, California 93106, United States
§*Physics Program, College of Creative Studies*
University of California, Santa Barbara, California 93106, United States
‖*Department of Materials Science and Engineering*
National University of Singapore, Singapore 117575.

E-mail: seshadri@mrl.ucsb.edu

Material descriptions

All structures reported were solved via single crystal X-ray diffraction with relevant crystallographic data summarized in Tables S1 and S2.

Table S1: Crystallographic Data for $(NH_4)_2PtI_6$ and $(MA)_2PtI_6$

Empirical Formula	$(NH_4)_2PtI_6$		$(CH_3NH_3)_2PtI_6$
Crystal habit, color	cubic, bronze		hexagonal, bronze
Crystal system	cubic	tetragonal	trigonal
Space group (#)	$Fm\bar{3}m$ (225)	$P4/mnc$ (128)	$R\bar{3}m$ (136)
Volume (Å^3)	1397(1)	681.6(1)	1250.5(2)
T (K)	290	100	273
a (Å)	11.179(4)	7.6446(5)	7.943(5)
b (Å)	11.179(4)	7.6446(5)	7.943(5)
c (Å)	11.179(4)	11.6625(9)	22.88(2)
α (°)	90	90	90
β (°)	90	90	90
γ (°)	90	90	120
Z	4	2	3
ρ (g mol^{-1})	984.51	985.52	1014.58
Dens. (g cm^{-3})	4.681	4.802	4.042
Abs. (mm^{-1})	23.257	23.834	19.491
F_{000}	1640	822	1284
Reflections (unique)	1167(175)	5177(532)	2643(423)
R_{int}	0.0523	0.0305	0.0443
R_1	0.0518	0.0291	0.0412
wR_R	0.0954	0.0513	0.1137
∂F (eÅ^{-3})	1.117 & −6.062	1.637 & −3.065	1.132 & −2.843
GOF	1.102	1.388	0.905

Figure S1(a) displays the 300 K structure of $(NH_4)_2PtI_6$ which crystallizes in the space group $Fm\bar{3}m$ and is isostructural to the VDHP K_2PtCl_6. In this structure, Pt and I are found on face-centered cubic lattices with ammonium cations in tetrahedral cavities.[1,2] Figure 1(b) presents the 100 K structure, space group $P4/mnc$. At low temperature $(NH_4)_2PtI_6$ distorts similar to other perovskites with an in phase octahedral rotation parallel to the c-axis, described by Glazer tilting nomenclature as a $a^0a^0c^+$ distortion.[3]

Figure S2 illustrates the 300 K structure of $(MA)_2PtI_6$, space group $R\bar{3}m$. We observe

Table S2: Crystallographic Data for $(FA)_2PtI_6$ and $(GUA)_2PtI_6$.

Empirical Formula	$[CH(NH_2)_2]_2PtI_6$		$[C(NH_2)_3]_2PtI_6$
Crystal habit, color	needle, bronze		block, bronze
Crystal system	monoclinic	tetragonal	hexagonal
Space group (#)	$P2_1/n$ (14)	$I4/m$ (87)	$P63mc$ (186)
Volume (Å^3)	855.0(2)	859(3)	924.8(3)
T (K)	100	350	100
a (Å)	7.679(2)	9.65(2)	9.369(2)
b (Å)	13.360(3)	9.65(2)	9.369(2)
c (Å)	8.572(2)	9.21(2)	12.164(2)
α (°)	90	90	90
β (°)	108.695(9)	90	90
γ (°)	90	90	120
Z	2	2	2
ρ (g mol^{-1})	1046.63	1041.59	1076.67
Dens. (g cm^{-3})	4.173	4.027	3.866
Abs. (mm^{-1})	19.516	18.923	17.588
F_{000}	892	882	924
Reflections (unique)	7379(2049)	956(459)	4907(1083)
R_{int}	0.0316	459	0.0335
R_1	0.0271	0.0736	0.0256
wR_R	0.0577	0.1798	0.0606
∂F ($e\mathring{A}^{-3}$)	1.313 & -2.026	1.775 & -1.275	1.992 & -1.654
GOF	1.235	1.104	1.047

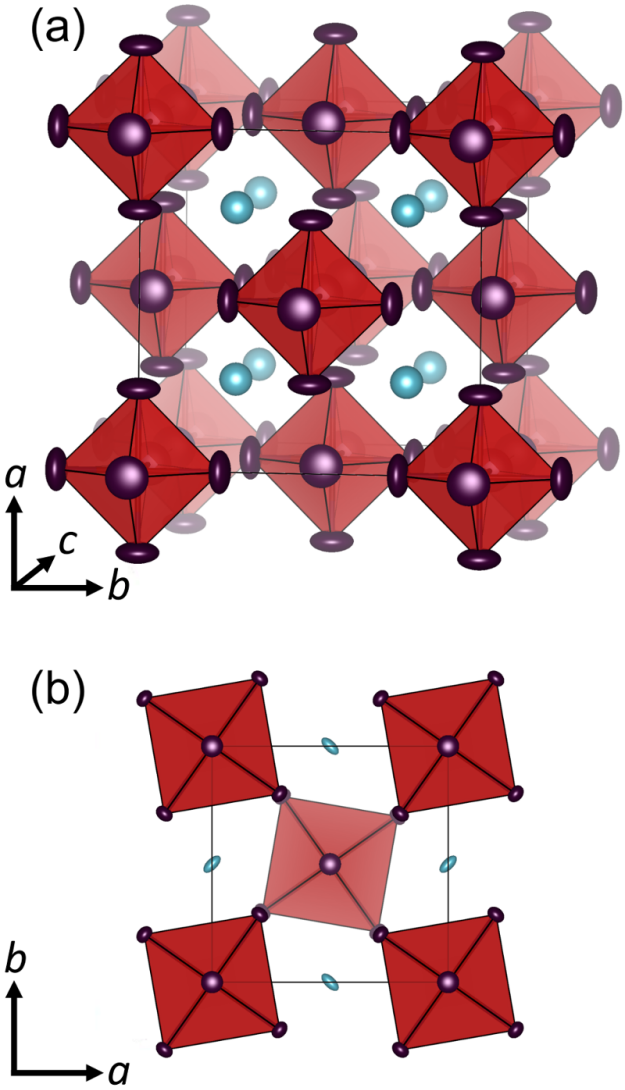

Figure S1: Crystal structure of $(NH_4)_2PtI_6$ with displacement ellipsoids (95% probability). (a) 300 K structure, viewed along c-axis, (b) 100 K structure, viewed along the c-axis to emphasize octahedral titling.

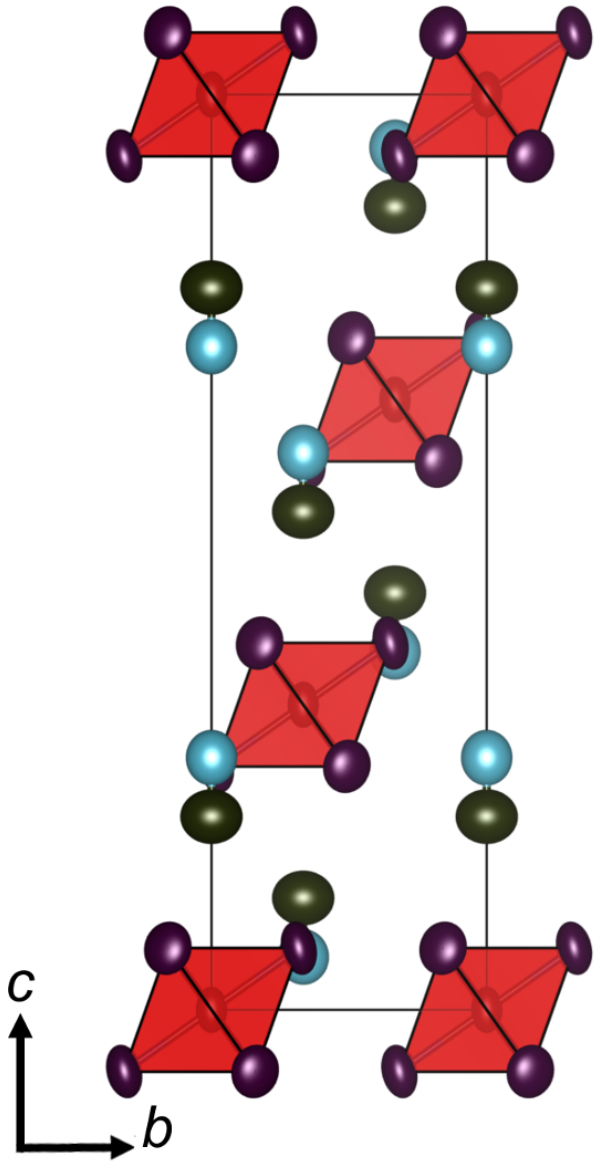

Figure S2: Crystal structure of $(MA)_2PtI_6$ at 300 K, with displacement ellipsoids (95% probability), viewed down along a-axis.

no first-order phase transition between 100 K and 480 K, though a second-order phase transition has previously been suggested at 134 K.[4,5] The platinum ions in $(MA)_2PtI_6$ are found on Wyckoff site $3a$ with site symmetry $\bar{3}m$, and iodide ions are found on Wyckoff site $18h$ with site symmetry $.m$. The methylammonium cations are modeled here as static molecules aligned parallel to the *c*-axis.

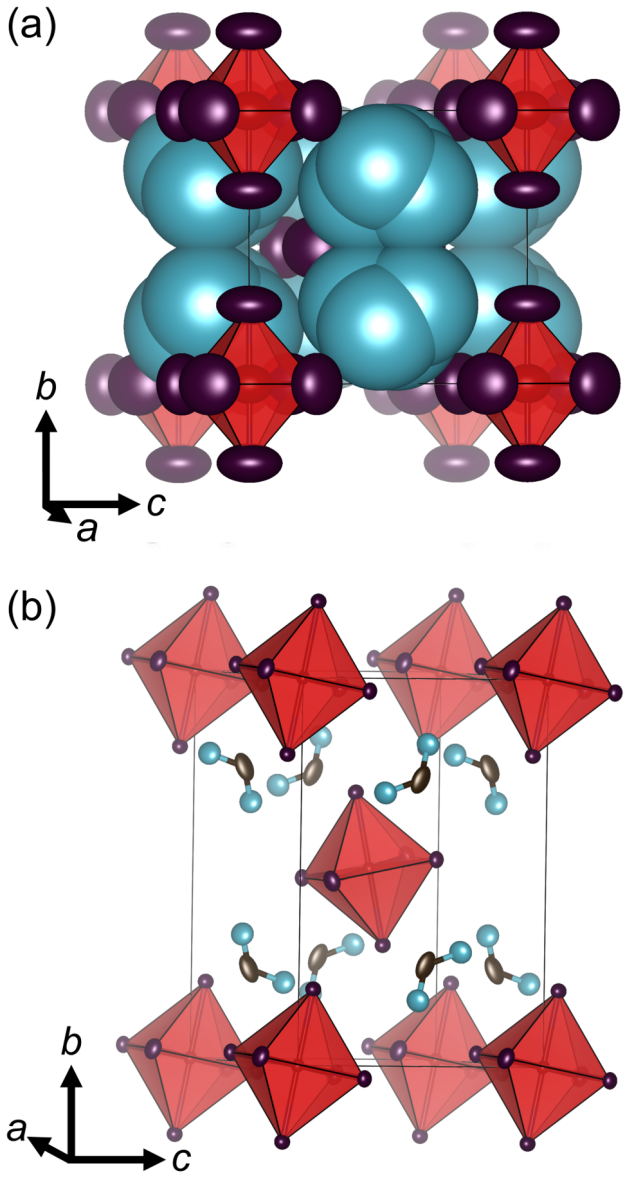

Figure S3: Crystal structure of $(FA)_2PtI_6$ with displacement ellipsoids (95% probability). (a) 340 K, viewed along a-axis. (b) 100 K and below, viewed down a-axis.

Figure S3 depicts the high temperature (340 K and warmer) and low temperature

(340 K to 100 K) structures of $(FA)_2PtI_6$. Some of the authors previously reported a compound of this empirical formula as isostructural to K_2PtI_6, but upon NMR analysis concluded this was incorrect. It was found that formamidinium ions degraded in solution (if the reaction temperature was brought above 70°C), yielding free NH_4^+ cations, which precipitate from solution in the form of $(NH_4)_2PtI_6$. If the solution is kept above 70°C for 20 minutes, $(NH_4)_2PtI_6$ is produced essentially pure. An erratum was submitted for the previous report.[8]

Figure S3(a) illustrates the high temperature phase of formamidinium platinum iodide, space group $I4/m$, viewed along the a-axis, depicting $[PtI_6]^{2-}$ octahedra and disordered formamidiniums. Platinum ions are found on Wyckoff site $2a$ with site symmetry $4/m..$, with two independent iodides residing on the $8h$ and $4e$ Wyckoff sites, site symmetry $m..$ and $4..$, respectively. Formamidinium cations are modeled as distorted tetrahedra. Figure S3(b) displays the low temperature structure of formamidinium platinum iodide, space group $P2_1/n$, illustrating canted octahedra and ordered formamidinium cations. The structure contains platinum ions on Wyckoff position $2a$ with site symmetry $\bar{1}$, and 3 independent iodide ions as well as formamidinium C and N atoms located on general positions $4e$. There are currently few reported formamidinium-containing VHDPs, but there are compounds that contain organic cations such as dimethylammonium which crystallize with similar structural motifs.[9,10]

Figure S4 displays the stable structure (between 100 K and 423 K) of $(GUA)_2PtI_6$, space group $P6_3mc$, viewed along the a-axis. Platinum ions are found on Wyckoff position $2b$ with site symmetry $3m.$ and iodide ions and carbon atoms are found on $6c$ positions, site symmetry $.m.$. There are two crystallographically distinct guanidinium cations within the unit cell of the compound, both of which are modeled here without disorder. The inorganic lattice is comprised of planes of similarly tilted $[PtI_6]^{2-}$ octahedra which alternate along the c-axis. $(GUA)_2PtI_6$ is similar to past reported guanidinium chloro- and bromometallate structures, though those reported consistently crystallize in the centrosymmetric space

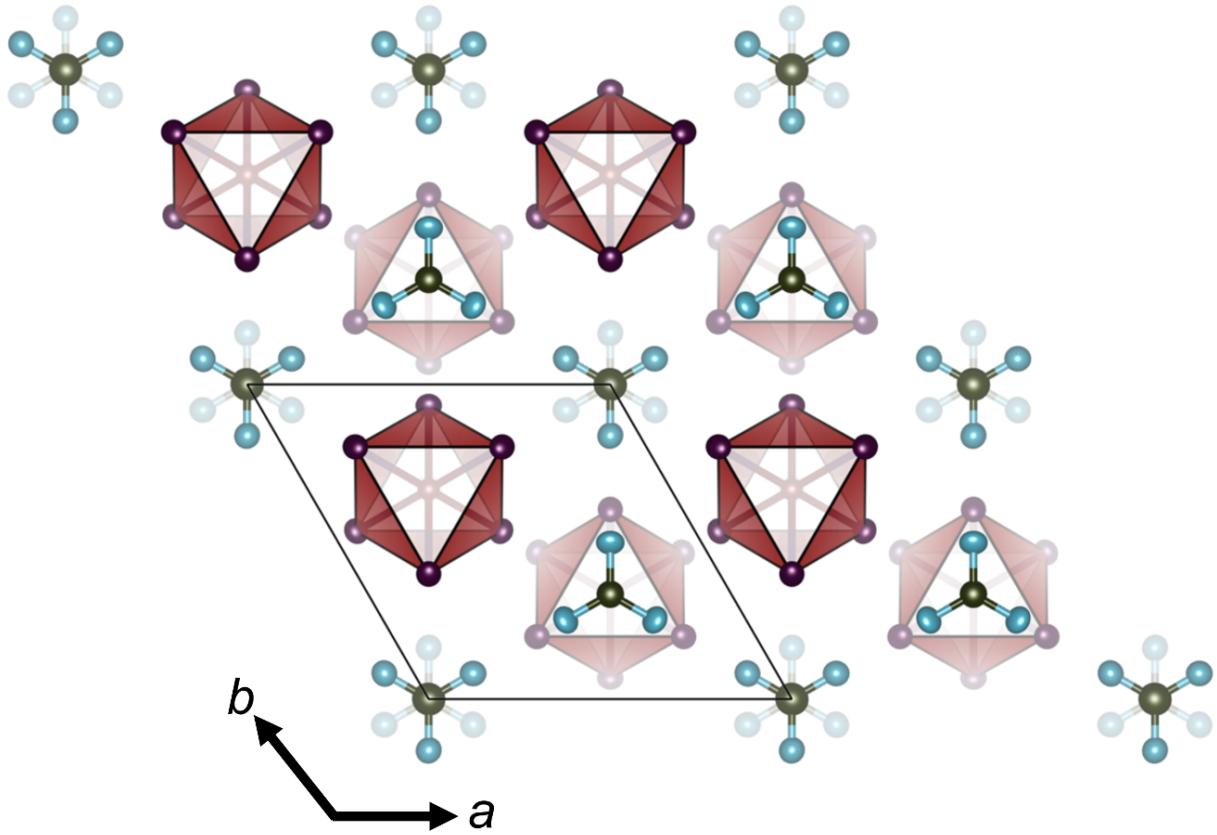

Figure S4: Crystal structure of $(GUA)_2PtI_6$ at 100 K, viewed along the c-axis, with displacement ellipsoids (95% probability).

group, $C2/m$.[11]

Powder X-ray Diffraction

Experimental laboratory PXRD data was Rietveld refined (without atomic occupancy) using room temperature single crystal diffraction as the structural comparison (Figure S5). The refinements indicate that the each bulk sample has unit cell parameters close to single crystal diffraction dimensions (Table S3 refined data, Tables S1 and S2 for single crystal data).

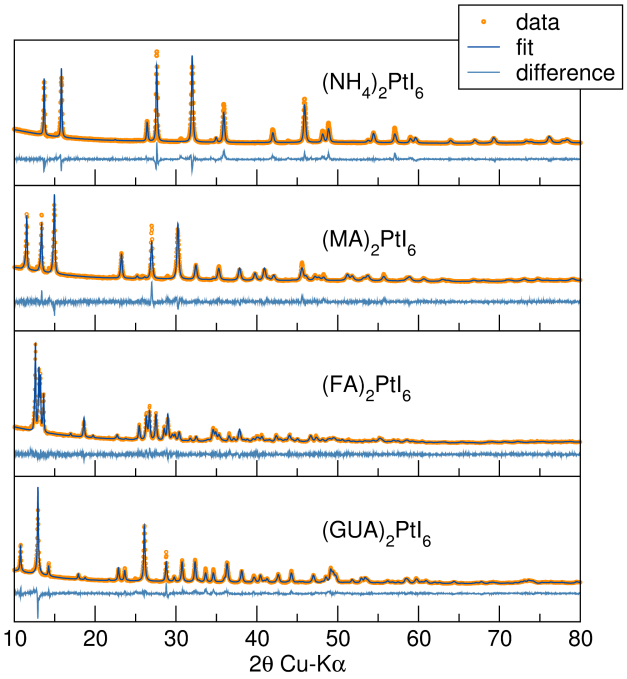

Figure S5: Rietveld refinements of the A_2PtI_6 compounds.

Table S3: Refined lattice parameters of A_2PtI_6 compounds.

Forumla	$(NH_4)_2PtI_6$	$(MA)_2PtI_6$	$(FA)_2PtI_6$	$(GUA)_2PtI_6$
a (Å)	11.175	7.955	7.790	9.424
b (Å)	11.175	7.955	13.512	12.377
c (Å)	11.175	22.918	8.630	9.424
α (°)	90	90	90	90
β (°)	90	90	109.1	90
γ (°)	90	120	90	120

Nuclear Magnetic Resonance (NMR)

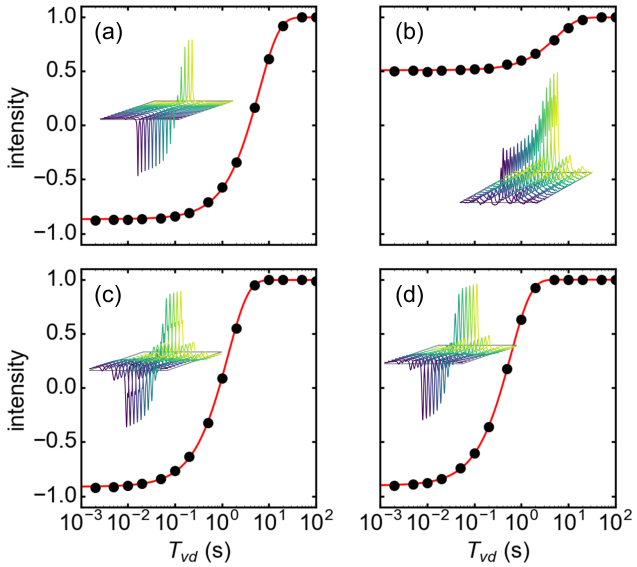

Figure S6: ^{1}H inversion recovery experiments of the A_2PtI_6 series. (a) $(NH_4)_2PtI_6$, (b) $(MA)_2PtI_6$, (c) $(FA)_2PtI_6$, (d) $(GUA)_2PtI_6$.

^{1}H inversion recovery experiments (Figure S6) were conducted to assess the degree of molecular motion in the A_2PtI_6 phases, and resulting longitudinal relaxation times, T_1, are given in Table 1 in the main text. We observe that T_1 is substantially longer in the ammonium and methylammonium phases, and reduced in the formamidinium and guanidinium phases.

^{1}H single-pulse NMR spectra under MAS for the A_2PtI_6 phases are presented in Figure S7. At these modest MAS speeds, ^{1}H dipolar interactions are only partially averaged out, and the three chemically distinct protons of the formamidinium ion cannot be re-

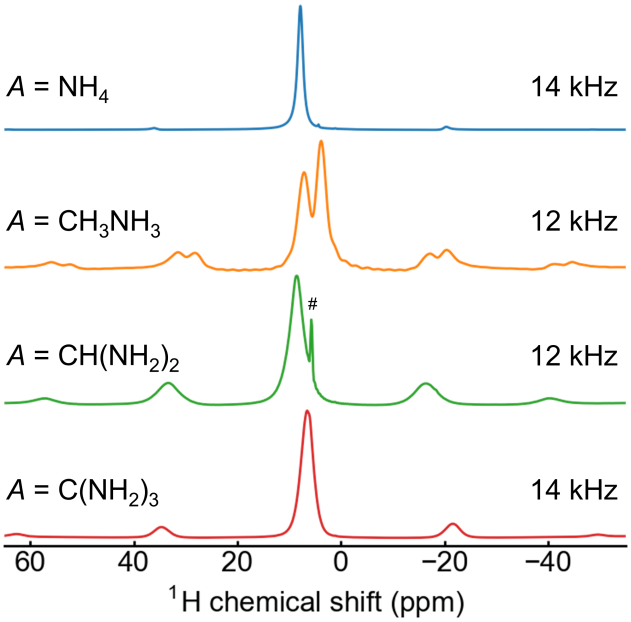

Figure S7: MAS ^{1}H NMR spectra of A_2PtI_6 phases, with spinning speed indicated. A small (3%), mobile impurity is evident in $(FA)_2PtI_6$ at 5.7 ppm, potentially from a NH_4 impurity generated through degradation of the formamidinium precursor. At this modest speed, strong ^{1}H dipolar interactions prevent resolution of the three chemically distinct protons on the formamidinium ion which are evident in solution. As $[NH_4]^+$ and $[GUA]^+$ each have one distinct proton, the broader signal for guanidinium suggests a reduced state of molecular motion.

solved.

Table S4: ^{195}Pt NMR lineshape parameters for A_2PtI_6 phases, Pt site symmetry from X-ray diffraction, and experimental and *ab initio* $[PtI_6]^{2-}$ octahedral volumes, V_{oct}. Ω = Guassian broadening. Ψ = Pt site symmetry

A	δ_{iso} **(ppm)**	δ_{CSA} **(ppm)**	η	Ω **(Hz)**	Ψ	**Expt.** V_{oct} **(Å)**	**Calc.** V_{oct} **(Å)**
NH_4	−5006	59	0.001	1963	$m\bar{3}m$	25.32	26.34
MA	−5478	166	0.106	2377	$\bar{3}m$	25.43	26.49
FA	−5518	218	−0.009	1066	$\bar{1}$	25.80	26.60
GA	−5926	196	0.224	1397	$3m.$	25.42	26.51

^{195}Pt lineshape and CSA parameters are given in Table S4, together with the Pt site symmetry from X-ray diffraction and the experimental and *ab initio* (vide infra) $[PtI_6]^{2-}$ octahedral volumes. The CSA parameters correlate well with Pt site symmetry, with the smallest δ_{CSA} for the highest site symmetry ($m\bar{3}m$), and the largest δ_{CSA} for the lowest Pt site symmetry ($\bar{1}$). While no CSA would be expected for Pt in the ammonium phase, due to the octahedral site symmetry, very small sidebands are observed. These likely arise from residual heteronuclear dipolar coupling, spin-orbit coupling, or other sources of broadening. The Gaussian broadening parameters extracted in lineshape fitting indicate broader lines in the ammonium and methylammonium phase. The origin of this behavior is not immediately apparent, as subsequent analysis of motion (*vide infra*) suggests that if anything, molecular motion is faster in these phases. In sum, no features are seen in NMR which suggest that the local environments of Pt deviate significantly from those in the crystallographic models.

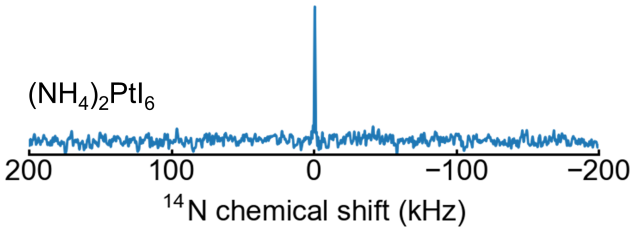

Figure S8: Spin-echo ^{14}N (S = 1) experiment for $(NH_4)_2PtI_6$, showing a narrow signal due to the tetrahedral molecular symmetry of the NH_4^+ cation.

Spin-echo ^{14}N (S = 1) experiments were additionally carried out (Figure S8) on the

A_2PtI_6 phases, leveraging the quadrupole moment as a probe of motion. A narrow signal was easily observed for $A = NH_4$ due to the tetrahedral molecular symmetry, while no signals were detected for the other three phases within one hour of acquisition. This result would be consistent with insufficiently rapid molecular motion to average out strong quadrupolar interactions, which are not already canceled due to the lower symmetry N environments in these molecules, though we cannot postulate more quantitative results without protracted experiments to acquire these (presumably) extremely broad signals.

Electronic Structure

The electronic band structures of the A_2PtI_6 phases, calculated within the framework of density functional theory (DFT), are presented in Figure 4 in the main text. Crystal structures were relaxed including semi-empirical van der Waals corrections, and the exchange-correlation energy was treated with the generalized gradient approximation (GGA; full computational details in the Methods section above).

The electronic bandgaps and line effective masses for electrons and holes (not the density of states effective masses) are given in Table S5, together with cell volumes from *ab initio* structure relaxation in Table S6. For the A_2PtI_6 phases, bandgaps and effective masses increase monotonically with countercation size, consistent with our discussion of intermolecular I–I contact. Bandgaps are indirect in all cases, with the valence band maxima occurring at the zone centers. No pattern in the locations of the conduction band minima is readily apparent without detailed analysis of the spatial relationship between the Brillouin zones of the different lattice types. Despite the use of van der Waals corrections, the DFT relaxed structures overestimate unit cell volumes by 9% to 17% (corresponding to 3% to 5% linear), in line with the known underbinding of the GGA.

For $(NH_4)_2PtI_6$, the valence band is $\sim$19 meV higher at Γ than at X, while the conduction band minimum occurs at X. This phase then has an indirect bandgap, but the direct

Table S5: Calculated electronic bandgaps (E_g) and line effective masses (m_e^*, m_h^*) for members of the A_2PtI_6 series. For line effective masses, the first Brillouin zone special point labels the band extremum, and the second special point indicates the direction from the extremum along which the dispersion is fitted.

Phase	E_g (eV)	VBM	CBM	m_e^* / m_0	m_h^* / m_0
$(NH_4)_2PtI_6$	0.55	Γ	X	X→Γ: 0.43	Γ→X (light): 0.64
				X→W: 0.39	Γ→X (heavy): 25.3
				X→U: 0.38	Γ→K (light): 0.64
					Γ→K (medium): 0.92
					Γ→K (heavy): 1.90
					Γ→L (light): 0.79
					Γ→K (heavy): 1.47
$(MA)_2PtI_6$	0.94	Γ	F	F→Q: 0.61	Γ→L: 1.29
				F→P_1: 0.74	Γ→Z: 1.29
					Γ→X: 2.30
$(FA)_2PtI_6$	1.00	Γ	D	D→Z: 0.78	Γ→Y: 1.75
				D→M: 0.87	Γ→X: 3.98
				D→Y: 0.61	Γ→Z: 1.74
$(GUA)_2PtI_6$	1.41	Γ	M	M→Γ: 3.46	Γ→M (light): 3.18
				M→K: 11.6	Γ→M (heavy): 6.08
				M→L: 32.2	Γ→K (light): 3.26
				K→M: 8.72	Γ→K (heavy): 5.97
				K→Γ: 3.41	Γ→A: 4.24
				K→H: 2.86	
				L→A: 2.05	
				L→H: 2.62	

Table S6: Calculated and experimental volume per formula unit (V / F.U.) for members of the A_2PtI_6 series.

Phase	**V / F.U. (Å^3), calc.**	**V / F.U. (Å^3), expt.**
$(NH_4)_2PtI_6$	382.2	350.25
$(MA)_2PtI_6$	475.1	416.83
$(FA)_2PtI_6$	501.4	427.50
$(GUA)_2PtI_6$	531.3	462.39

transition at X is only slightly higher in energy. The valence band is quite flat along the Γ−X line, much like the isotypic Cs_2SnI_6.[12–14]

For $(MA)_2PtI_6$, the valence band is ∼70 meV higher at Γ than at F, while the conduction band minimum occurs at F. This phase then has an indirect bandgap, but the direct transition at F is only slightly higher in energy.

For $(FA)_2PtI_6$, the conduction band is ∼30 meV lower at D than at Γ. The valence band is ∼25 meV higher at Γ than at X, and ∼25 meV higher at Γ than at X. Accordingly, the band gap is indirect, but direct transitions at both Γ and D are only slightly higher in energy.

For $(GUA)_2PtI_6$, the conduction band is nearly degenerate in energy (<10 meV difference) at the M, K, and L points, with the energy at M being the lowest by a slight margin. In contrast, all other local maxima of the valence band are 10s of meV lower in energy than the valence band maximum at Γ. Once again, the bandgap is indirect, but direct transitions at K and L are only somewhat higher in energy.

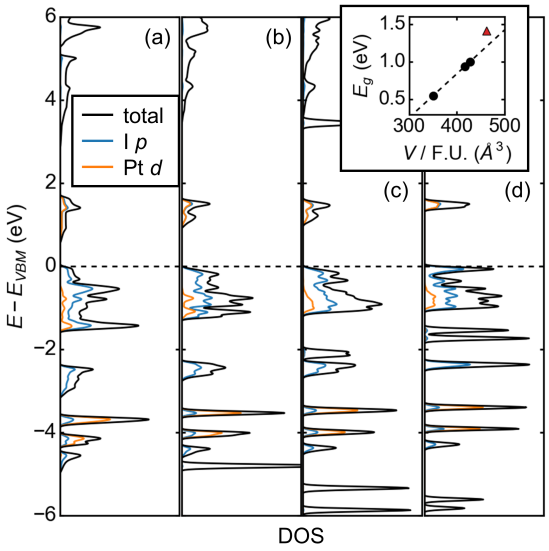

Figure S9: Electronic densities of states (GGA-PBE) for A_2PtI_6 phases, including orbital projections of the I *p* and Pt *d* states. Energies are referenced to the valence band maximum for each phase. Inset: The calculated bandgap is correlated with cell volume for the A = (NH_4), MA, and FA phases (•), which are increasingly distorted versions of the same anti-fluorite structure type. The transition to a different $[PtI_6]^{2-}$ packing arrangement for A = GA (△) widens the bandgap relative to this trend.

The electronic densities of states calculated for the A_2PtI_6 phases, as well as the correlation between bandgap and unit cell volume, are presented in Figure S9. Tracking the position of the localized I *s* states (not shown, ∼12 eV below the VBM) relative to the VBM suggests the VBM drops relative to the vacuum with increasing countercation size (and increasing bandgap). In essence, the band widths are reduced while the band centers remain nearly constant, as expected for phases with somewhat ionic Pt–I bonding and varying degrees of intermolecular I–I contact. For the distorted VHDP ammonium, methylammonium, and formamidinium phases, there is a very strong correlation between bandgap and cell volume (Figure S9 inset), while the different anion packing of the guanidinium phase results in a larger bandgap than expected from this trend.

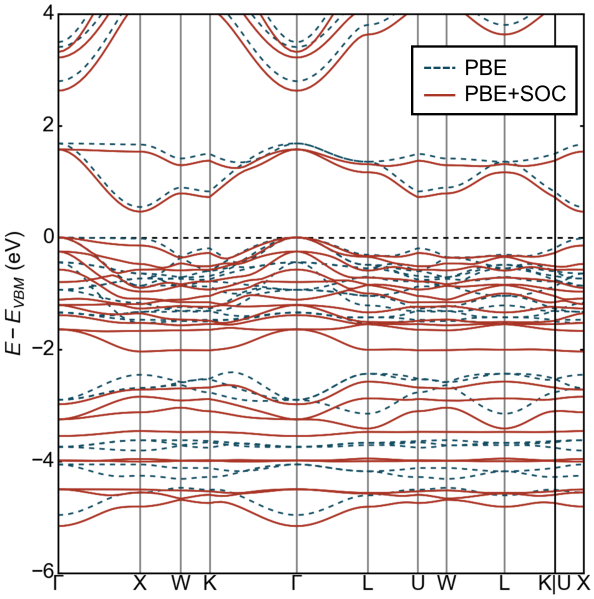

Figure S10: Comparison of PBE to PBE+SOC calculations for $(NH_4)_2PtI_6$.

A calculation was performed on $(NH_4)_2PtI_6$ with both PBE and PBE+SOC, which indicated that the effect of spin-orbit coupling is modest (Figure S10).

Thermogravimetric Analysis (TGA)

Thermogravimetric analysis, presented in Figures S11 - S14, show similar degradation temperatures for each member of the A_2PtI_6 series.

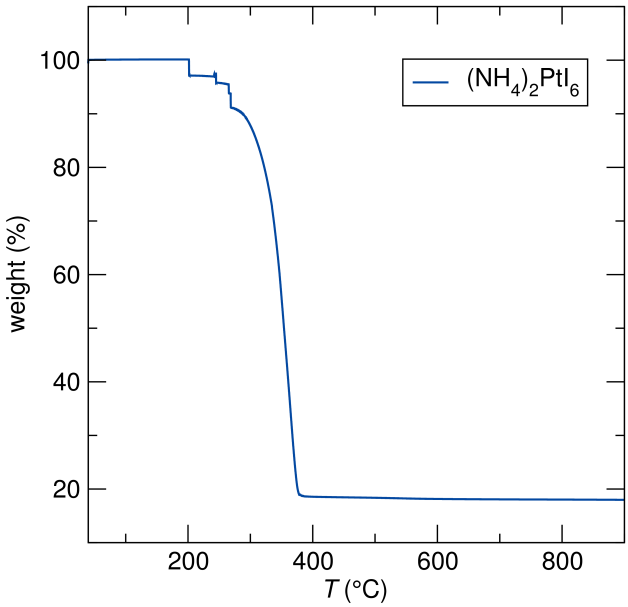

Figure S11: TGA data for $(NH_4)_2PtI_6$ from room temperature to 900°C.

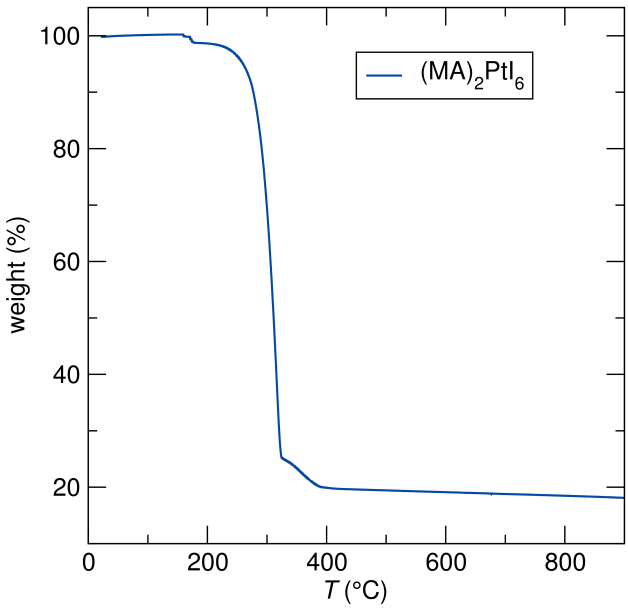

Figure S12: TGA data for $(MA)_2PtI_6$ from room temperature to 900°C.

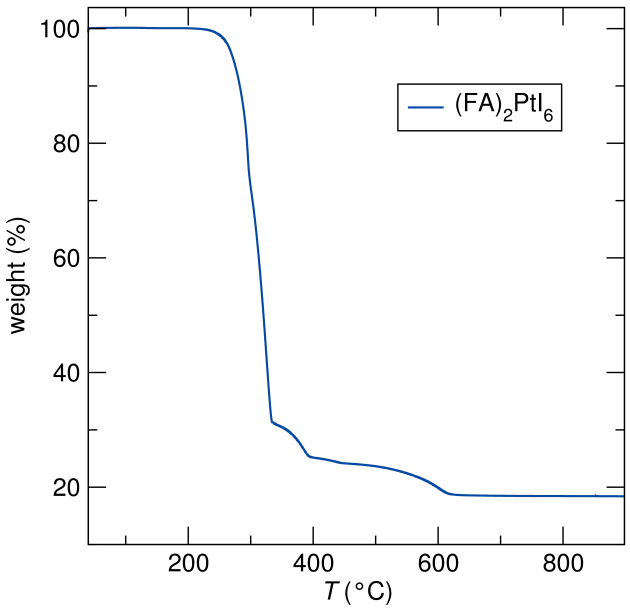

Figure S13: TGA data for $(FA)_2PtI_6$ from room temperature to 900°C.

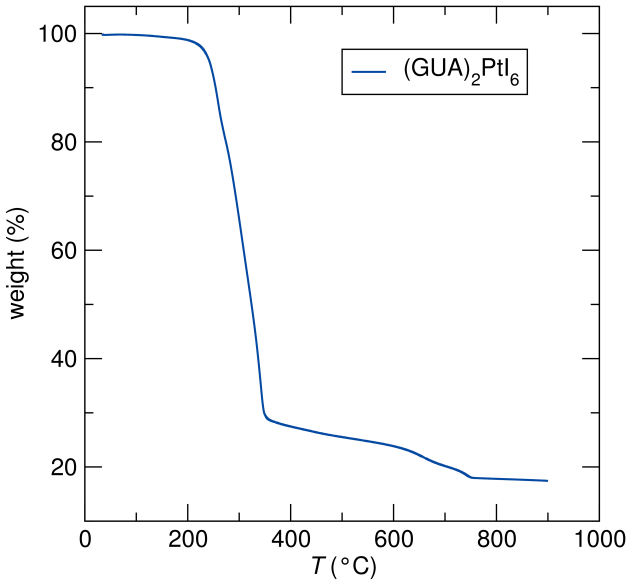

Figure S14: TGA data for $(GUA)_2PtI_6$ from room temperature to 900°C.

Differential Scanning Calorimetry (DSC)

Differential scanning calorimetry of the A_2PtI_6 is presented in Figures S15 - S18.

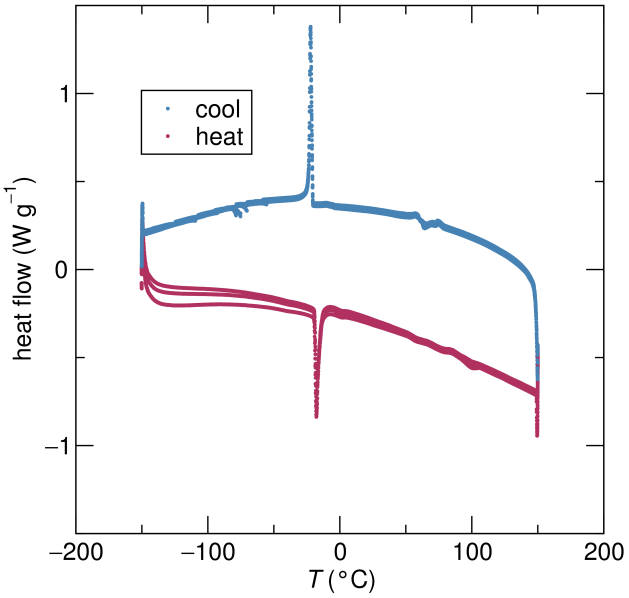

Figure S15: DSC data for $(NH_4)_2PtI_6$ between −150 °C and 150 °C. A first order phase transition can be seen at −20°C.

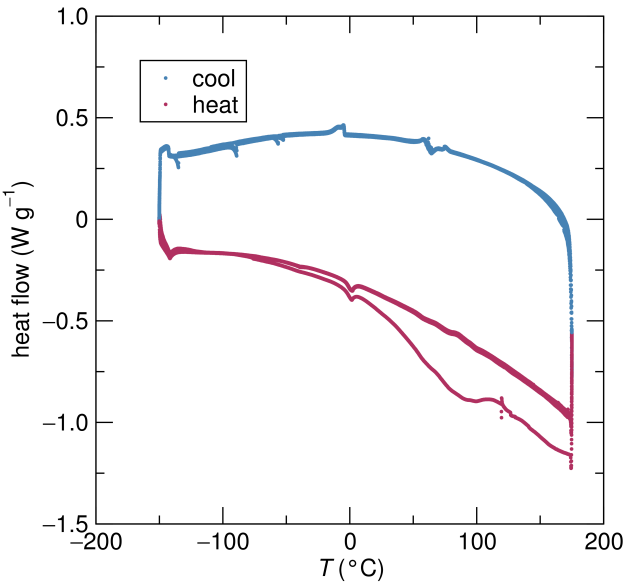

Figure S16: DSC data for $(MA)_2PtI_6$ between −150 °C and 175 °C. No first order phase transition is observed.

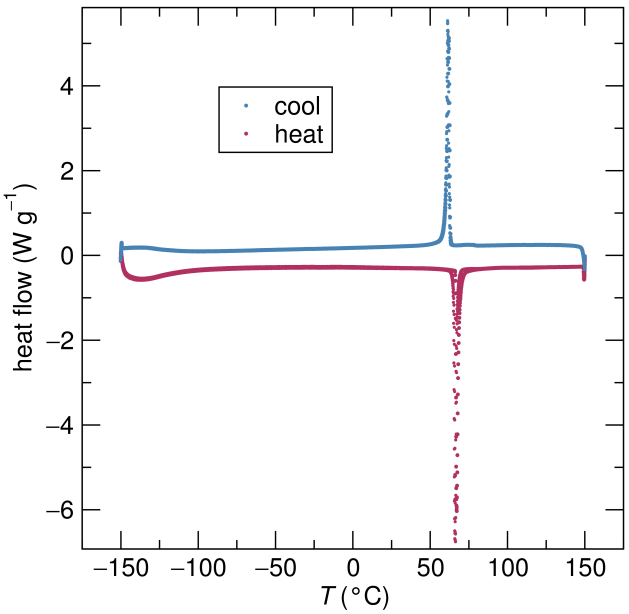

Figure S17: TGA data for $(FA)_2PtI_6$ between −150 °C and 150 °C. A first order phase transition is observed near 63°C.

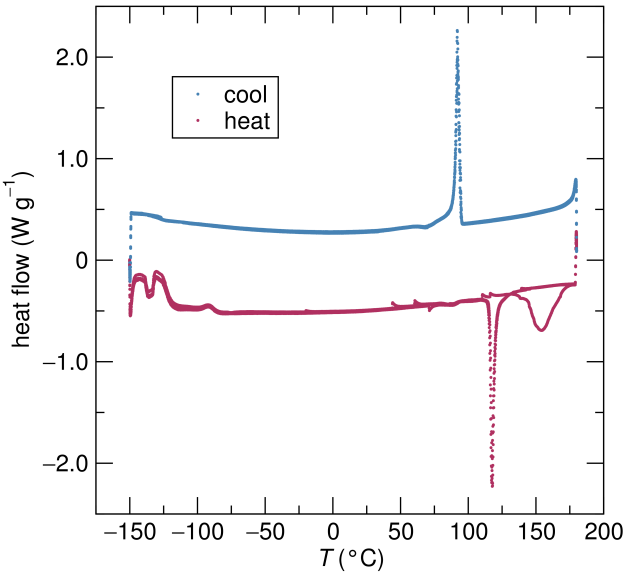

Figure S18: TGA data for $(GUA)_2PtI_6$ between −150 °C and 175 °C. There is a second order phase transition near 100°C associated with increased molecular motion of the guanidinium cation.

References

(1) Ewing, P. J.; Pauling, L. XIII. The Crystal Structure of Potassium Chloroplatinate. *Z. Kristallogr.* **1928**, *68*, 223–230.

(2) Williams, R. J.; Dillin, D. R.; Milligan, W. O. Structure refinement of potassium chloroplatinate by powder and single-crystal methods. *Acta Crystallogr. Sect. B-Struct. Sci.* **1973**, *29*, 1369–1372.

(3) A. Glazer. The classification of tilted octahedra in perovskites. *Acta Crystallogr. Sect. B-Struct. Sci.* **1972**, *28*, 3384–3392.

(4) Kume, Y.; Ikeda, R.; Nakamura, D. Structural Phase Transition in Various Methylammonium Hexahalometallates(IV) as Studied by the NQR of Halogens. *J. Magn. Reson.* **1979**, *33*, 331–344.

(5) Nakamura, D. Nuclear Quadrupole Resonance Studies of Structural and Magnetic Phase Transitions. *J. Mol. Struct.* **1983**, *111*, 341–356.

(6) Larson, A. C.; Von Dreele, R. B. "General Structure Analysis System (GSAS)", Los Alamos National Laboratory Report LAUR, **2000**, 86–748

(7) Toby, B. H. *EXPGUI*, a Graphical User Interface for GSAS. *Appl. Cryst.* **2001**, *34*, 210–213.

(8) Evans, H.A.; Schueller, E.C.; Smock, S.R.; Wu, G.; Seshadri, R.; Wudl, F. Perovskite-Related Hybrid Noble Metal Iodides: Formamidinium Platinum Iodide $[(FA)_2Pt^{IV}I_6]$ and Mixed-Valence Methylammonium Gold Iodide $[(MA)_2Au^{I}Au^{III}I_6]$. *Inorg. Chim. Acta* **2017**, *468*, 280–284.

(9) Ishida. H.; Kashino, S. Bis(dimethylammonium) Hexachlorotellurate(IV). *Acta Cryst.* **1998**, *C54*, 1811–1813.

(10) Ghozlen, M. H. B.; Daoud, A. Dimethylammonium Hexaehlorostannate(IV). *Acta Cryst.* **1981**, *B37*, 1415–1416.

(11) Ishida, H.; Furukawa, Y.; Kashino, S. Bis(guanidinium) hexachlorostannate(IV). *Acta Cryst.* **1999**, *55*, 1995–1997.

(12) Lee, B.; Stoumpos, C. C.; Zhou, N.; Hao, F.; Malliakas, C.; Yeh, C.-Y.; Marks, T. J.; Kanatzidis, M. G.; Chang, R. P. H. Air-Stable Molecular Semiconducting Iodosalts for Solar Cell Applications: Cs_2SnI_6 as a Hole Conductor. *J. Am. Chem. Soc.* **2014**, *136*, 15379–15385.

(13) Maughan, A. E.; Ganose, A. M.; Bordelon, M. M.; Miller, E. M.; Scanlon, D. O.; Neilson, J. R. Defect Tolerance to Intolerance in the Vacancy-Ordered Double Perovskite Semiconductors Cs_2SnI_6 and Cs_2TeI_6. *J. Am. Chem. Soc.* **2017**, *138*, 8453–8464.

(14) Saparov, B.; Sun, J-P.; Meng, W.; Xiao, Z.; Duan, H-S.; Gunawan, O.; Shin, D.; Hill, I. G.; Yan, Y.; Mitzi, D. B. Thin-Film Deposition and Characterization of a Sn-Deficient Perovskite Derivative Cs_2SnI_6. *Chem. Mater.* **2016**, *28*, 2315–2322.